CrossMark

The effects of monsoons and climate teleconnections on the Niangziguan Karst Spring discharge in North China

Juan Zhang[1] · Yonghong Hao[2] · Bill X. Hu[3,4] · Xueli Huo[5,6] · Pengmei Hao[7] ·
Zhongfang Liu[8]

Abstract Karst aquifers supply drinking water for 25 % of the world's population, and they are, however, vulnerable to climate change. This study is aimed to investigate the effects of various monsoons and teleconnection patterns on Niangziguan Karst Spring (NKS) discharge in North China for sustainable exploration of the karst groundwater resources. The monsoons studied include the Indian Summer Monsoon, the West North Pacific Monsoon and the East Asian Summer Monsoon. The climate teleconnection patterns explored include the Indian Ocean Dipole, E1 Niño Southern Oscillation, and the Pacific Decadal Oscillation. The wavelet transform and wavelet coherence methods are used to analyze the karst hydrological processes in the NKS Basin, and reveal the relations between the climate indices with precipitation and the spring discharge. The study results indicate that both the monsoons and the climate teleconnections significantly affect precipitation in the NKS Basin. The time scales that the monsoons resonate with precipitation are strongly concentrated on the time scales of 0.5-, 1-, 2.5- and 3.5-year, and that climate teleconnections resonate with precipitation are relatively weak and diverged from 0.5-, 1-, 2-, 2.5-, to 8-year time scales, respectively. Because the climate signals have to overcome the resistance of heterogeneous aquifers before reaching spring discharge, with high energy, the strong climate signals (e.g. monsoons) are able to penetrate through aquifers and act on spring discharge. So the spring discharge is more strongly affected by monsoons than the climate teleconnections. During the groundwater flow process, the precipitation signals will be attenuated, delayed, merged, and changed by karst aquifers. Therefore, the coherence coefficients between the spring discharge and climate indices are smaller than those between precipitation and climate indices. Further, the fluctuation of the spring discharge is not coincident with that of precipitation in most situations. Karst spring discharge as a proxy can represent groundwater resource variability at a regional scale, and is more strongly influenced by climate variation.

✉ Bill X. Hu
bill.x.hu@gmail.com

1 College of Mathematical Science, Tianjin Normal University, Tianjin 300387, China

2 Tianjin Key Laboratory of Water Resources and Environment, Tianjin Normal University, Tianjin 300387, China

3 Department of Ecology, Jinan University, Guangzhou 510632, Guangdong, China

4 Department of Earth, Ocean and Atmospheric Sciences, Florida State University, Tallahassee, FL 32306, USA

5 College of Global Change and Earth System Science (GCESS), Joint Center for Global Change Studies, Beijing Normal University, Beijing 100875, China

6 College of Urban and Environmental Science, Tianjin Normal University, Tianjin 300387, China

7 School of Computer Software, Tianjin University, Tianjin 300072, China

8 State Key Laboratory of Marine Geology, Tongji University, Shanghai 200092, China

1 Introduction

Karst terrains cover 7–12 % of the Earth's continental surface area, and karst aquifers supply freshwater resources for

about 25 % of the world population entirely and partly (Ford and Williams 2007; Hartmann et al. 2014). Karst aquifers are generally considered to be particularly vulnerable to climate change (Leibundgut 1998). Despite the vital contributions to freshwater supply, the study on the relationship between climate change and karst groundwater resource is very limited, which restricts the ability of government to plan and manage karst groundwater resource. Karst groundwater depletion occurs in many places throughout the world, such as the United States (Beynen et al. 2007), France (Gams et al. 1993), Italy (Sauro 1993), Germany (Heinz et al. 2008), Serbia (Jemcov 2007), and China (Guo et al. 2005). In the northern China, karst spring discharges have been declining due to climate change and anthropogenic activities since the 1950s. Many large karst springs have become dry, such as Jinci Springs, Lancun Springs, Gudui Springs, Heilongdong Springs, and Zhougong Springs (Liang et al. 2008).

The Niangziguan Karst Spring (NKS) complex is the largest karst springs in North China with average discharge of 9.81 m^3/s (1959–2011). The NKS Basin is surrounded by an impermeable boundary, and precipitation infiltration is the main source recharging groundwater (Han et al. 1993). The only natural discharge outlet of the groundwater system in the basin is NKS (Liang et al. 2008). Therefore, understanding the relations between the large scale climate variation and spring discharge would be helpful for water resource management in the NKS Basin.

The magnitude and frequency of climate change have increased since the beginning of last century (IPCC 2007, 2012). The relation between climate change and groundwater resource is complex (Taylor et al. 2013). In recent years, the effects of teleconnections/large scale climate phenomena on groundwater have been received more attentions. Holman et al. (2011) demonstrated that groundwater levels at three boreholes in different aquifers across UK were correlated with North Atlantic ocean–atmosphere teleconnection patterns based on a wavelet coherence analysis. Gurdak et al. (2007) identified the importance of interannual to interdecadal climate variability on water-flux estimation in thick vadose zones and provided better understanding of the climate-induced variations responsible for the observed deep infiltration and chemical-mobilization events. To better understand groundwater recharge in Canada, Tremblay et al. (2011) used correlation, wavelet analysis and wavelet transform coherence methods to investigate the relations between climatic indices and groundwater level in three Canadian regions. Groundwater levels in the three regions were affected by different teleconnection patterns. The groundwater level in Prince Edward Island region was mostly influenced by the Arctic Oscillation (AO) and the North Atlantic Oscillation (NAO), the groundwater level in southern Manitoba in the vicinity of Winnipeg region was affected by the Pacific-North American Pattern (PNA),

and the groundwater level in Vancouver Island region was impacted by NAO, AO and the multivariate E1 Niño Southern Oscillation (ENSO). Furthermore, Perez-Valdivia et al. (2012) used Spearman rank correlation and spectral analyses to assess the effects of climate teleconnection patterns on the groundwater levels in Canadian Prairies, and found that the groundwater level varied with 2–10-year and 18–22-year oscillations in response to the influences of ENSO and the Pacific Decadal Oscillation (PDO), respectively. Kuss and Gurdak (2014) used singular spectrum analysis, wavelet coherence analysis, and lag correlation to quantify the effects of teleconnection patterns on principal aquifers in the U.S. Their study results indicate that groundwater levels are partially controlled by inter-annual to multi-decadal climate variability and are not solely a function of temporal patterns in pumping. Although those studies have linked large scale climate patterns to groundwater level, relations between large-scale climate pattern variability and karst groundwater are not well studied.

The purpose of this project is to study the effects of monsoons [i.e. the Indian Summer Monsoon (ISM), the West North Pacific Monsoon (WNPM), and the East Asian Summer monsoon (EASM)], and teleconnection patterns [i.e. the Indian Ocean Dipole (IOD), ENSO, and PDO] on NKS discharge, in North China. Different from previous studies in which groundwater level is used as proxy to reflect the groundwater system condition, we use spring discharge as proxy in this study to describe the groundwater condition. Because a spring is a natural discharge point of an aquifer, and its discharge variation reflects the combined information of aquifer permeability and groundwater level variability over a regional scale, while groundwater level change only represents groundwater variation in a local scale.

2 Study area and data

2.1 Study area

The NKS complex is located in the Mianhe Valley, Taihang Mountains, Eastern Shanxi Province, and extends about 7 km along the Mianhe riverbank (Fig. 1). The main aquifers of the basin are comprised of Cambrian and Ordovician karstic limestone, Quaternary sandstone and unconsolidated sediments. The limestone and Quaternary sediment aquifers are hydraulically connected (Han et al. 1993). Karst groundwater flows from the north and the south toward NKS in the east. At the Mianhe Valley, the groundwater flows upward due to a geologic unconformity, where groundwater perches on low-permeable strata of dolomite, and eventually intersects the land surface and discharges at the NKS (Hu et al. 2008). The western part of the basin is higher than the eastern part, with the general topography of

Fig. 1 The location and digital elevation model of Naingziguan Springs Basin
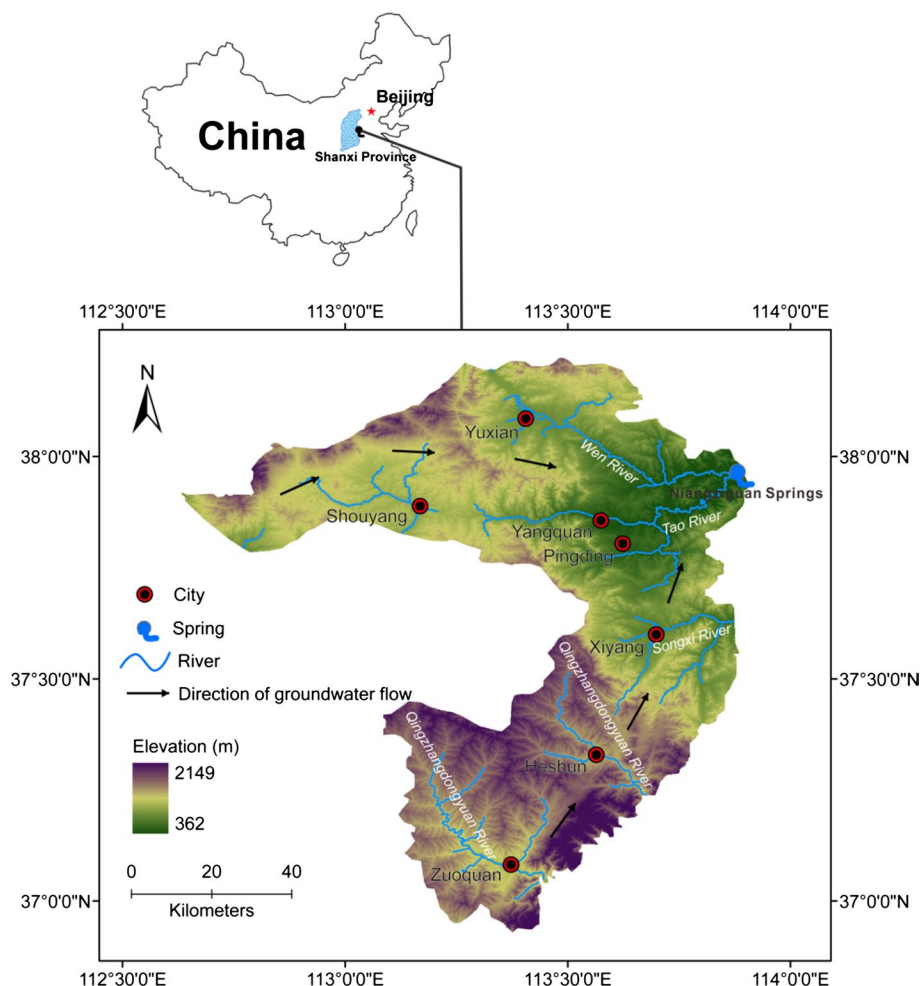
the basin inclining to the east. The Mianhe Valley, where NKS is located, has the lowest elevation in the NKS Basin, ranging from 360 to 392 m above mean sea level (Fig. 1). The main outcropping strata in the NKS Basin are Ordovician carbonate rocks, Carboniferous coal seams, Permian and Triassic detrital formations, and Quaternary deposits.

The NKS Basin is in the warm temperate zone with a semiarid continental monsoon climate. The largest total annual precipitation recorded was 844 mm in 1963 and the smallest is 292 mm in 1972. The average annual precipitation is 530 mm based on the record from 1958 to 2010. As much as 60–70 % of annual precipitation usually occurs from July to September.

The NKS is the largest karst springs in North China. According to records from 1959 to 2011, the NKS complex has an annual average discharge of 9.81 m^3/s, a maximum monthly flow rate of 18.10 m^3/s (in September 1985), and a minimum monthly flow rate of 4.69 m^3/s (in March 1995). NKS receives water from a catchment with the area of 7394 km^2, covering the city of Yangquan, and the counties of Pingding, Heshun, Zuoquan, Xiyang, Yuxian, and Shouyang (Fig. 1). The NKS Basin is surrounded by

impermeable boundaries and the only discharge outlet of groundwater system in the basin is NKS. So precipitation is the primary source of recharge to the aquifers in the basin (Han et al. 1993). The annual recharge rate is 27 % in the exposed karst region, and 10 % in the buried karst region in the NKS Basin (Yuan 1982).

2.2 Data

Monthly NKS discharge data from January 1959 to December 2011 were collected from the Niangziguan gauge station in the Mianhe River. The monthly precipitation data were obtained from six meteorological stations (Yangquan City, Yuxian County, Shouyang County, Xiyang County, Heshun County and Zuoquan County) in the NKS Basin from January 1959 to December 2010. In this study, we used the principal component analysis method to analyze the precipitation data from six stations, and the first principle component obtained could explain 90.29 % of the variance.

Monthly mean data for monsoon indices of ISM and WNPM are available from the Monsoon Monitoring

website, http://apdrc.soest.hawaii.edu/projects/monsoon/. Monthly mean data of EASM is collected from National Oceanic and Atmospheric Administration's (NOAA) website (http://www.cpc.ncep.noaa.gov/products/Global_Monsoons/Asian_Monsoons/Figures/Index/EastAsiaPacific/oct.shtml). Monthly data for teleconnection patterns of ENSO are obtained from the website of the Climate Prediction Center of National Weather Service, http://www.cpc.ncep.noaa.gov, whereas the PDO is available from the Joint Institute of the Study of the Atmosphere and Ocean, the University of Washington (JISAO), http://jisao.washington.edu/pdo/PDO.latest. The IOD index from HadISST data set is defined as the SST anomaly difference between the western equatorial Indian Ocean (10°N–10°S, 50°E–70°E) and the south eastern equatorial Indian Ocean (0°N–10°S, 90°E–110°E).

3 Methods

3.1 Principal component analysis

Principal component analysis (PCA) is a multivariate statistical method which can be used to simplify multiple related variables to a few unrelated variables and reveals the relationship between the variables. The fundamental idea is to reduce the dimension from a simplified variance and covariance by the structure. PCA is used to extract the important information from observations by reducing the noises (Takio 2014). The number of principal components is less than or equal to the number of original variables. This transformation is defined in such a way that the first principal component has the largest possible variance (that is, accounts for as much of the variability in the data as possible), and each succeeding component in turn has the highest variance possible under the constraint that it is orthogonal to uncorrelated components. The principal components are orthogonal because they are the eigenvectors of the covariance matrix, which is symmetric. PCA is sensitive to the relative scaling of the original variables.

3.2 Pre-processing

Hydrological processes have been significantly affected by human activities including groundwater pumping (Milly et al. 2008). A systematic method to investigate the influence of atmospheric circulation on spring discharge must provide a method to separate a natural process from anthropogenic influence (Hanson et al. 2004). A general method to remove anthropogenic impacts on a process is to subtract the trend by human activity from the observed data (Perez-Valdivia et al. 2012). In the NKS Basin, the spring discharge has decreased for many years, but the declining rate is gradually alleviated recently due to the recent implementation of sustainable exploration and policy of groundwater resource protection (China Preparatory Committee for United Nations Conference on Sustainable Development 2012). In this study, the trend of Niangziguan Spring discharge is fitted by an exponential function. By subtracting the exponential function from the spring discharge, we acquire the residual spring discharge (i.e. detrended spring discharge), which successfully separates the human effect from a natural process of the spring discharge.

3.3 Continuous wavelet transform

A wavelet series is a representation of a square-integral function by a certain orthonormal series generated by a wavelet, and wavelet transformation is one of the most popular candidates of the time–frequency transformation. A wavelet function $\psi(t)$, defined as $\int_{-\infty}^{+\infty} \psi(t)dt = 0$, is a special kind of the waveform which has a finite length and a zero average value. Wavelet analysis is used to analyze irregular and asymmetrical data in a time scale through decomposing the signals into a series of wavelet functions, a main difference from the trigonometric functions used in classic Fourier analysis (Kriechbaumer et al. 2014). These wavelet functions are made by translating and stretching a mother wavelet function on the scale, so it is most suitable to use the wavelet function to imitate the signals from local properties. Each wavelet is derived from a mother wavelet $\psi(t)$ by expansion and translation to form $\psi_{a,\tau}(t)$,

$$\psi_{a,\tau}(t) = \frac{1}{\sqrt{a}}\psi\left(\frac{t-\tau}{a}\right), \quad a, \tau \in R; a > 0 \tag{1}$$

where a is the scale expansion factor, τ is the time shift factor and t is dimensionless time; ψ is the mother wavelet function, R represents the real number set.

There are many mother wavelet functions that could be selected, such as Mexican Hat wavelet, Morlet wavelet, Haar wavelet and so on. In this study, we use the complex non-orthogonal Morlet wavelet function. The function has been used to generate robust results in analysis of time series records (Grinsted et al. 2004; Appenzeller et al. 1998; Gedalof and Smith 2001). The Morlet wavelet is defined as,

$$\psi_0(t) = \pi^{-1/4}e^{i\omega_0 t}e^{-t^2/2} \tag{2}$$

where ω_0 is dimensionless frequency and t is dimensionless time. In general, the Morlet wavelet (with $\omega_0 = 6$) is a good choice since it provides a good balance between time and frequency localization.

Continous wavelet transform (CWT) of a time series $(x_t, t = 1, \ldots, N)$ with uniform time step Δt, is defined as the convolution of x_t with the scaled and transformed wavelet $\psi_0(t)$,

$$W_x(a, \tau) = \sqrt{\frac{\Delta t}{a}} \sum_{t=1}^{N} x_t \psi_0^* \left[\frac{(t-\tau)\Delta t}{a} \right] \qquad (3)$$

where $*$ denotes the complex conjugate; a is the scale expansion factor, τ is the time shift factor and t is dimensionless time. $W_x(a, \tau)$ reflects the essential characteristics of a time series x_t, which is projected into a two-dimensional time frequency space.

The CWT has an edge artifact problem because the wavelet is not completely localized in time. Therefore, a Cone of Influence (COI) is introduced to solve the edge effect problem, in which the wavelet power $|W_x(a, \tau)|^2$ caused by a discontinuity at the edge has dropped to e^{-2} of the value at the edge.

3.4 Cross wavelet transform

The cross wavelet transform (XWT) between two time series x_t and y_t is defined as,

$$W_{xy}(a, \tau) = W_x(a, \tau)W_y^*(a, \tau) \qquad (4)$$

where $*$ denotes the complex conjugate; a is the scale expansion factor, τ is the time shift factor. $W_x(a, \tau) = |W_x(a, \tau)| \exp(\Phi_x(a, \tau))$ because they are complex numbers. $|W_x(a, \tau)|$ denotes the wavelet amplitude, $\Phi_x(a, \tau)$ is the absolute phase. Further, we define the cross wavelet power as $|W_{xy}(a, \tau)|$, and it depicts the cross covariance between the two time series. The relative phase difference between the two time series can be calculated as,

$$\Phi_{xy}(a, \tau) = \tan^{-1}\left(\frac{I(S(a^{-1}W_{xy}(a, \tau)))}{R(S(a^{-1}W_{xy}(a, \tau)))} \right) \in [-\pi, \pi] \quad (5)$$

where S represents a smoothing operator, a is the scale expansion factor, τ is the time shift factor. It should be pointed out that this definition depends essentially on the action of the smoothing operator on the various wavelet spectra. I and R indicate the imaginary and real part of $W_{xy}(a, \tau)$, respectively. Areas which have two time series in the time–frequency plane exhibit common power, and the consistent phase behavior indicates a relationship between the signals.

3.5 Wavelet coherence

XWT reveals the areas with high common power. The wavelet coherence is a method for analyzing how coherent the XWT in a time frequency space. The wavelet coherence coefficient is defined by Torrence and Compo (1998) as,

$$R^2(a, \tau) = \frac{|S(a^{-1}W_{xy}(a, \tau))|^2}{S(a^{-1}|W_x(a, \tau)|^2) \cdot S(a^{-1}|W_y(a, \tau)|^2)} \qquad (6)$$

where $R^2(a, \tau)$ takes a value between 0 and 1, and is used to measure the wavelet coherence as a localized correlation coefficient in time frequency space. S is a smoothing operator and is defined as,

$$S(W) = S_{scale}(S_{time}(W(a, \tau))) \qquad (7)$$

where S_{scale} and S_{time} represent smoothing along the wavelet scale axis and in time scale, respectively. For the Morlet wavelet, Torrence and Webster (1999) defined a suitable smoothing operator as,

$$S_{time}(W)|_a = \left(W(a, \tau) \cdot c_1^{\frac{-\tau^2}{2a^2}} \right) \Big|_a ,$$
$$S_{scale}(W)|_\tau = (W(a, \tau) \cdot c_2 \Pi(0.6a))|_\tau \qquad (8)$$

where c_1 and c_2 are normalization constants and Π is the rectangle function; a is the scale expansion factor; τ is the time shift factor. The wavelet is stretched in time by varying its scale (a). The factor of 0.6 is the empirically determined scale decorrelation length for the Morlet wavelet (Torrence and Compo 1998). In practice both convolutions are done discretely and therefore the normalization coefficients are determined numerically.

The statistical significance level of the wavelet coherence is estimated using Monte Carlo methods. The estimation requires the order of 1000 surrogate data set pairs with the same AR (1) coefficients as the input data sets. We calculate the wavelet coherence for each pair. The significance level for each scale is estimated using only values outside the COI. The number of scales per octave should be high enough to capture the rectangle shape of the scale smoothing operator while minimizing computing time. Our pretrial study results indicate 12 scales per octave are required. The 5 % significance level against red noise is taken into our analysis after the calculations.

3.6 Global coherence

The global wavelet coherence coefficient at a certain scale, a, is defined as time-averaged wavelet coherence coefficients,

$$\overline{R}^2(a) = \frac{1}{n} \sum_{\tau=1}^{n} R^2(a, \tau) \qquad (9)$$

where a is the scale parameter in the frequency domain; τ is the location parameter in the time domain; n is the number

of points in the time series (Torrence and Compo 1998; Partal and Kucuk 2006).

The global coherence coefficient is used to estimate the correlation between two time series on different scales, which is helpful to examine the characteristic periodicities (Torrence and Compo 1998; Labat 2010).

The Matlab package of wavelet coherence provided by Grinsted et al. (2004) is used for the calculation in this study, and the package is available from the URL http://noc.ac.uk/using-science/crosswavelet-wavelet-coherence.

4 Results

4.1 Principal component analysis of precipitation data set

Monthly precipitation data were collected from six meteorological stations located in Yangquan City, Yuxian County, Shouyang County, Xiyang County, Heshun County and Zuoquan County over the NKS Basin (Fig. 1). To obtain the precipitation characteristics of the basin (i.e. the representative precipitation series of the basin), the PCA is used to analyze the interrelationships among six precipitation sequences. We acquire a representative precipitation sequence that could be used to explain these variables, and it is called the principal component which has a minimum loss of original precipitation information.

The PCA results of precipitation data set which consists of six precipitation sequences are listed in Table 1. The variance proportion of the first principle component Y1 is 90.29 %, which is greater than the required 80 %. Therefore, the first principal component of the precipitation data set is used as the precipitation sequence to represent precipitation in the NKS Basin.

4.2 Data preprocessing for Niangziguan Karst Springs discharge

As shown in Fig. 2a, an exponential function fits the long-term trend of Niangziguan Springs discharge, and the function is,

$$y_{trend} = 14.9 \exp(-0.00147t) \tag{10}$$

where y_{trend} denotes the long-term trend of the spring discharge; t is time.

The residual of the spring discharges over the time process is obtained by subtracting the exponential function from the spring discharge, and it is is assumed to be affected only by natural conditions (Fig. 2b).

$$Q_t = x_t - y_{trend} \tag{11}$$

where x_t denotes the spring discharge; Q_t represents the detrended spring discharge.

Table 1 Principal component analysis of precipitation data set

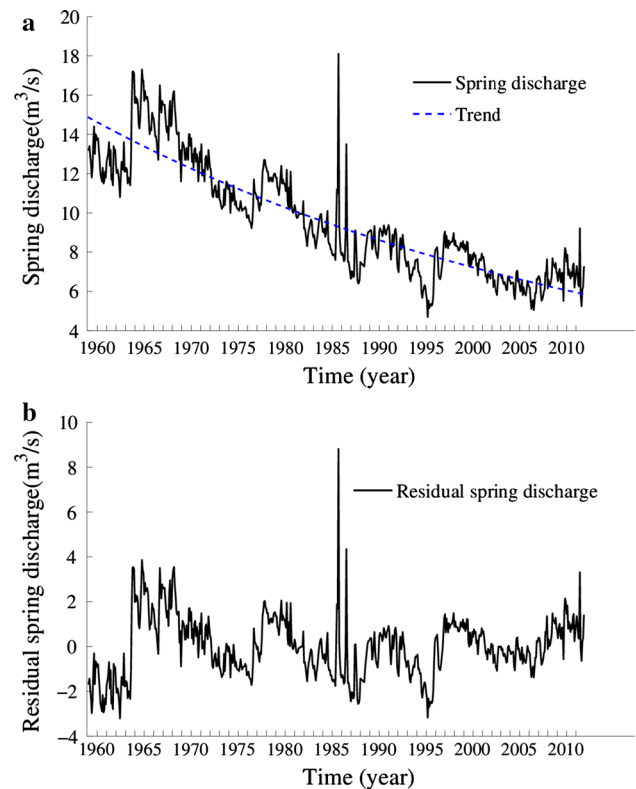| Principal components	Latents	Variance proportion (%)
Y1	17,083	90.29
Y2	800	4.23
Y3	451	2.38
Y4	238	1.25
Y5	198	1.05
Y6	151	0.80

Fig. 2 Niangziguan Springs discharge and the detrended spring discharge

Hereinafter the detrended spring discharge is referred to as spring discharge and the following analysis is based on the detrended data.

4.3 CWT for climate phenomena, precipitation and the spring discharge

To better understand the variabilities of the climate indices, precipitation and the spring discharge, we analyze their oscillations using CWT (Figs. 3, 4, 5). For the monsoon indices, the obvious 0.5-year and 1-year periodicities are observed for ISM (Fig. 3a), and apparent periodicity of 1-year is observed for WNPM and EASM (Fig. 3b, c). For the large-scale climate patterns, the periodicities of

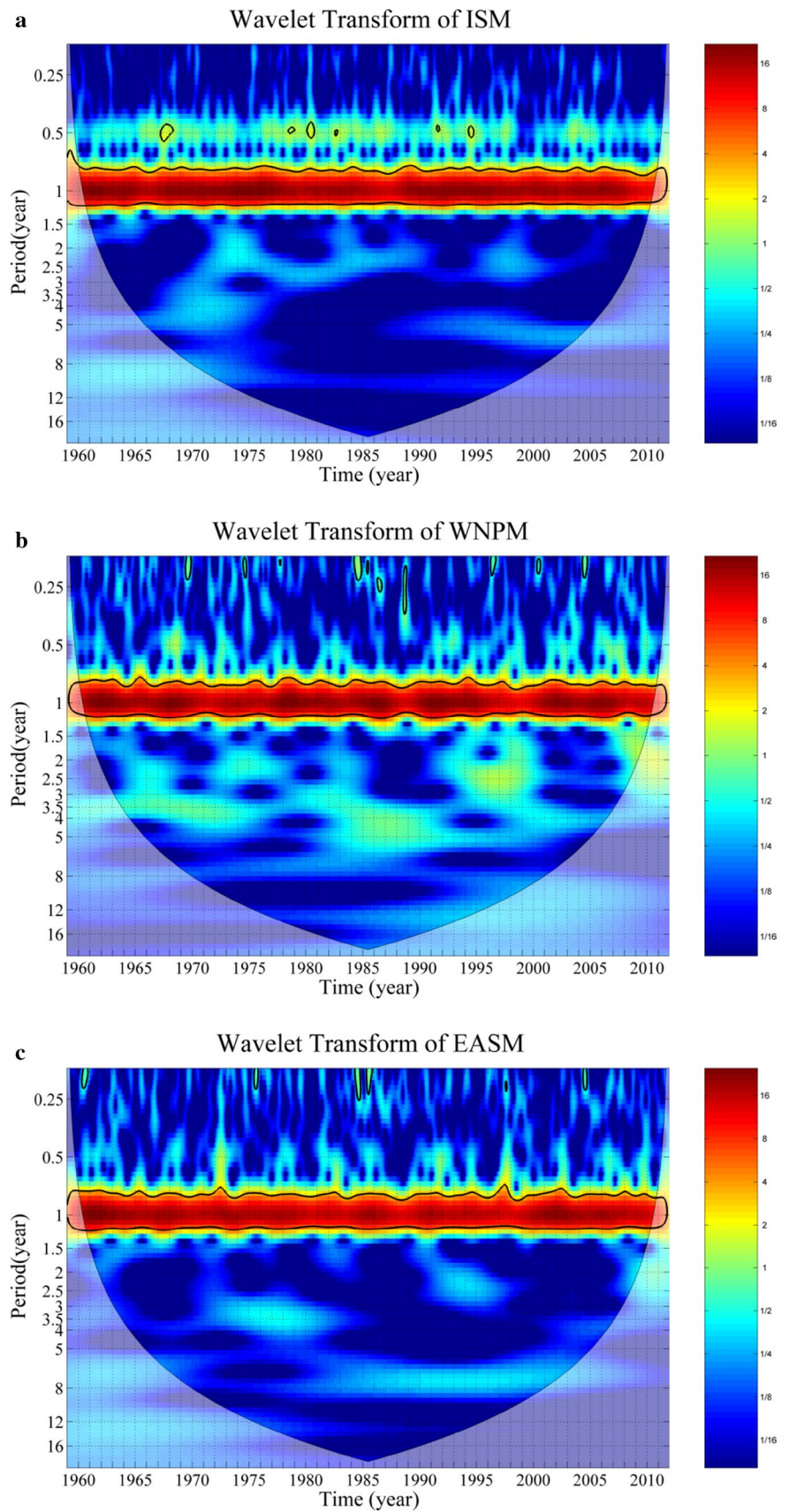**Fig. 3** The wavelet transform
for the monsoon indices

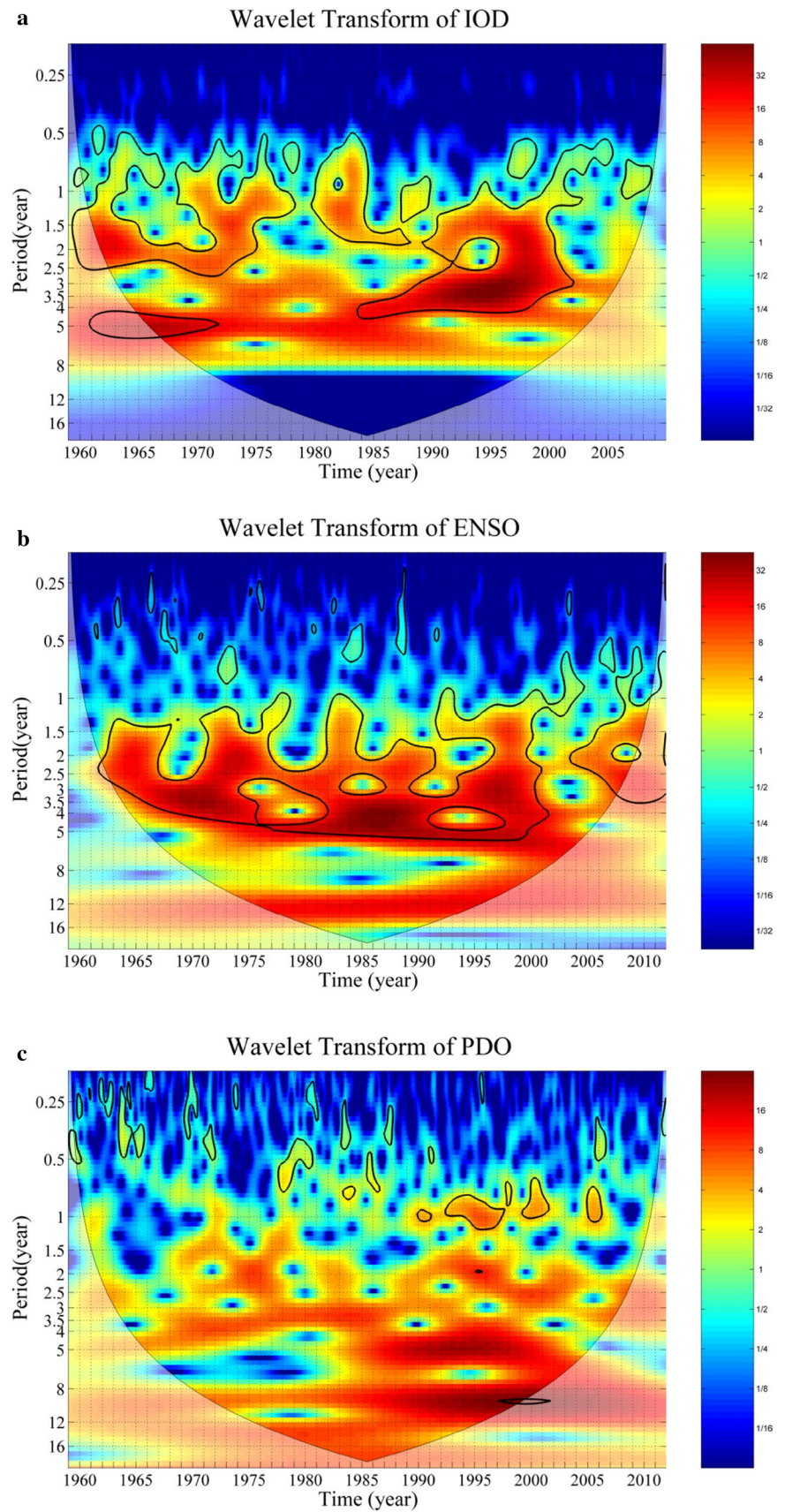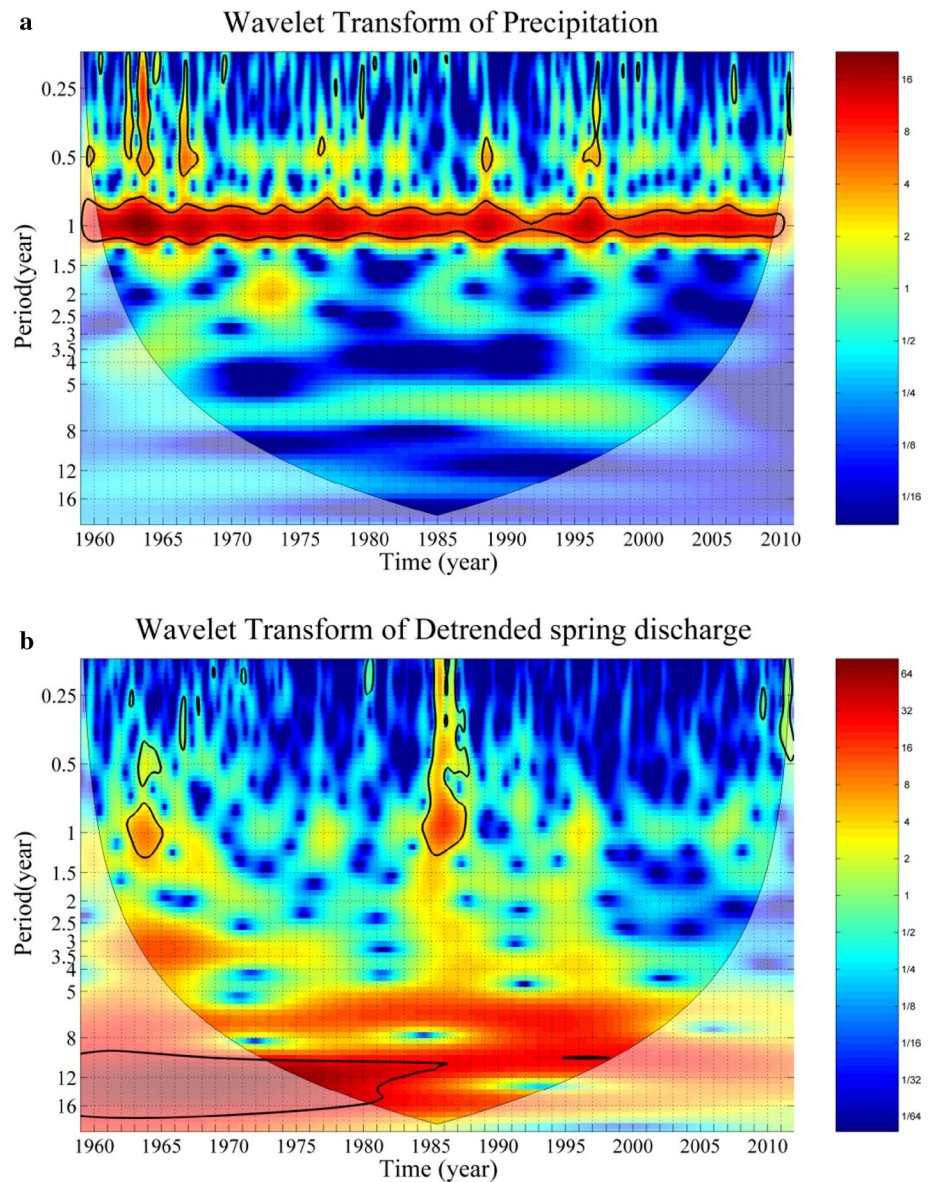**Fig. 4** The wavelet transform
for the climate teleconnection
indices

2–4-year, and 2–6-year are observed for IOD, and ENSO (Fig. 4a, b). The periodicities of 10–23-year can be seen for PDO (Fig. 4c). Simultaneously the periodicities of 0.5-, 1-, and 7-year are observed for precipitation (Fig. 5a), and 1-, 3.5-, 7-, and 16-year are observed for the NKS discharge (Fig. 5b). From the results, we can find that the signals between climate indices, precipitation and the spring discharge have resonance, respectively. For example, ISM, WNPM and EASM resonate with precipitation and the spring discharge at the periodicity of 1-year. Therefore further investigation is needed to reveal the relations between climate indices, precipitation and the spring discharge.

4.4 Coherence between precipitation and climate phenomena

We calculate the wavelet coherence coefficients and global coherence coefficients between monthly precipitation and climate indices, and the results are shown in Figs. 6 and 7.

The wavelet coherence between precipitation and ISM (Fig. 6a) shows a continuously significant region (surrounded by thick black contour) at 1-year time scale. The intermittent significant regions during 1960–1964, 1966–1980, 1981, 1988–1990, 1993–1996 and 2000–2010 at 0.5-year time scale are apparent. The intermittent

Fig. 6 The wavelet coherence between precipitation and the monsoon indices
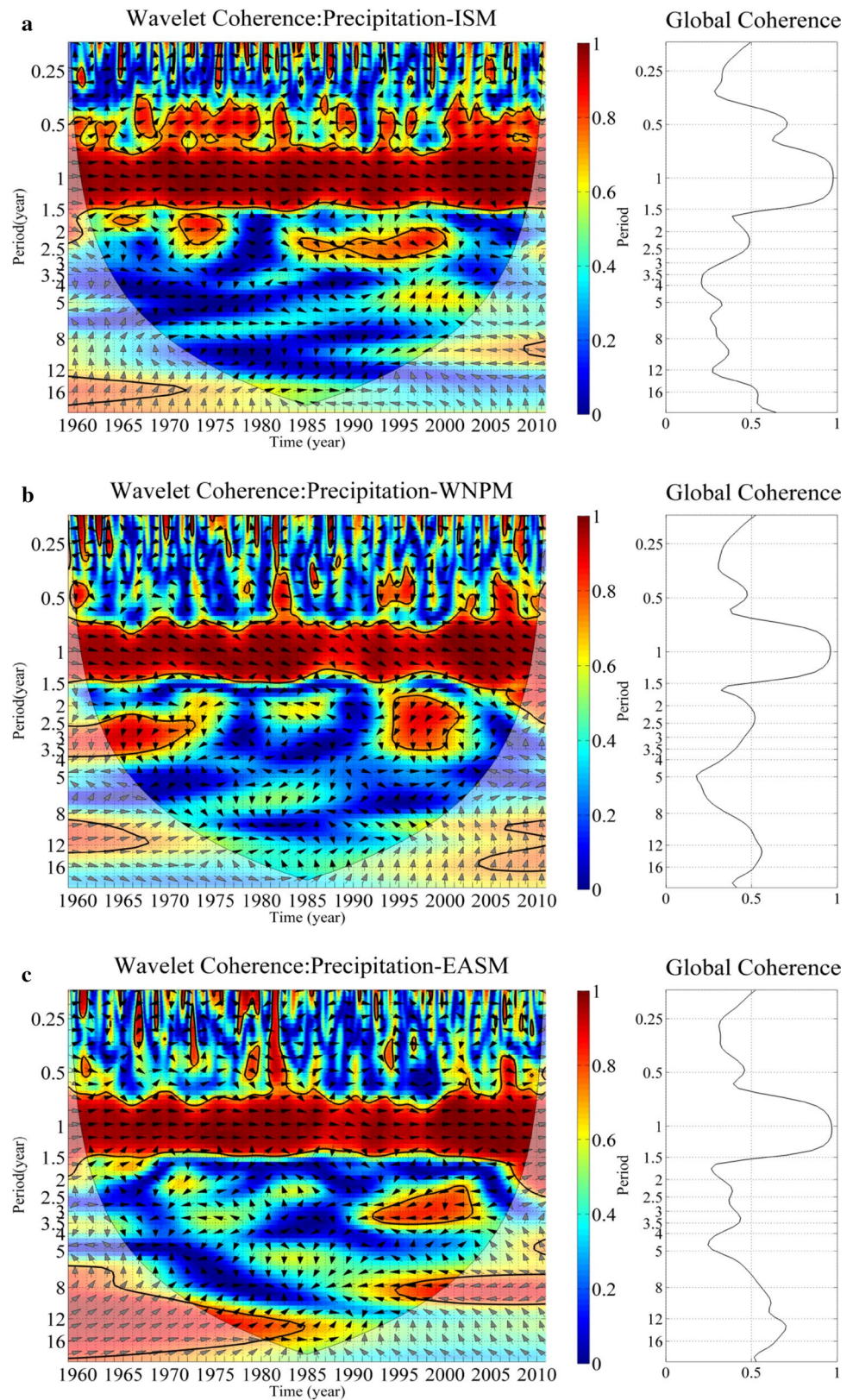
significant regions at 2.5-year time scale are mainly found in 1971–1976 and 1984–2000. All the significant regions show in-phase relation over all periods except 1984–2000,

which means ISM affects precipitation positively. The in-phase relation indicates a complete positive correlation. The peak of global coherence between precipitation

Fig. 7 The wavelet coherence between precipitation and the climate teleconnection indices
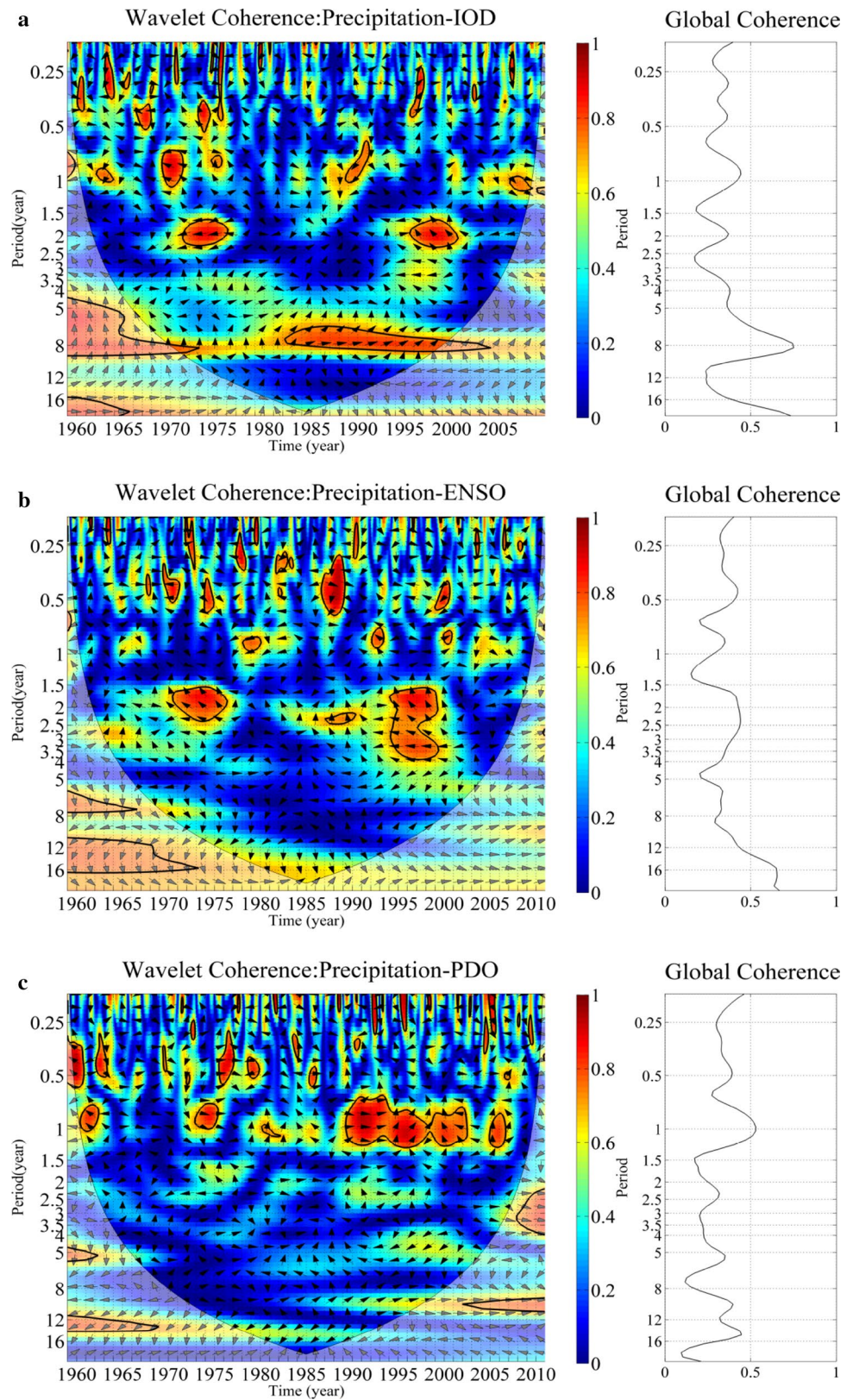
and ISM are 0.97, 0.71, and 0.49 at 1-, 0.5-, and 2.5-year time scales, respectively (Table 2). Although there is a peak at the time scale of 16-year, it is ignored because the significant region is located out of COI. We think ISM affects precipitation mainly at 1-, 0.5-, and 2.5-year time scales.

Table 2 Peaks of global coherence coefficients between precipitation and climate indices

Time scale of significant region (years)	0.5	1	2	2.5	3.5	8
Monsoon						
ISM	0.71	0.97	–	0.49	–	–
WNPM	0.47	0.96	–	0.52	–	–
EASM	0.46	0.97	–	–	0.44	–
Climate teleconnection						
IOD	–	0.44	0.37	–	–	0.75
ENSO	0.42	0.35	–	0.44	–	–
PDO	0.39	0.53	–	–	–	–

Similarly, the wavelet coherence between precipitation and WNPM (Fig. 6b) shows a continuously significant region at 1-year time scale. The intermittent significant regions at 0.5-year time scale are obvious during time periods of 1960, 1981–1983, 1993–1997, 2002 and 2005–2008. The apparently significant regions during 1963–1973 and 1994–2002 are observed at 2.5-year time scale. The significant regions at 1-year time scale show in-phase relation over all periods, which means that WNPM affects precipitation positively. The peaks of global coherence between precipitation and WNPM are 0.96, 0.47, and 0.52 at 1-, 0.5-, and 2.5-year time scales, respectively (Table 2). Although there is a peak at the time scale of 14-year, the significant region is located out of COI, so it is neglected. The WNPS affects precipitation mainly at 1-, 0.5-, and 2.5-year time scales.

Figure 6c shows a continuous significant region at 1-year scale band between precipitation and EASM. The intermittent significant regions at 0.5-year scale are also obvious during time periods of 1960, 1972, 1978–1979, 1981–1982, 1993 and 2006–2007, respectively. The apparent significant regions during 1992–2002 are observed at 3.5-year scale band. The significant regions at 1-year scale show in-phase relation over all periods, meaning that EASM affects precipitation positively. The in-phase correlation is also found during the periods of 1981–1982 and 2006–2007 at 0.5-year scale band. The maximum global coherence coefficient corresponding to the significant region is 0.97 at 1-year scale band. The global coherence coefficients at 0.5- and 3.5-year scales peaking locally are 0.46 and 0.44, respectively (Table 2).

The wavelet coherence between precipitation and IOD (Fig. 7a) shows intermittent significant regions at 8-year time scale during 1971–1973, and 1982–1999. The intermittent significant regions at 1 year time scale are observed during the time periods of 1962–1965, 1969–1971, 1988–1991 and 2005–2008. The obvious intermittent significant regions at 2-year time scale are still observed during

1971–1977 and 1995–2001. The peaks of global coherence between precipitation and IOD are 0.75, 0.44, and 0.37 at 8-, 1-, and 2-year time scales, respectively (Table 2).

The wavelet coherence between precipitation and ENSO (Fig. 7b) shows that there are three groups of intermittent significant regions located at time scales of 0.5-year (1970, 1974, 1987–1989 and 1999–2001), 1-year (1978–1980, 1992–1994 and 2000) with anti-phase correlation in 1978–1980, and 2.5-year (1978–1980, 1992–1994 and 2000). The anti-phase relation indicates completely negative correlation. Although there are significant regions at 7- and 16- year time scales, they are neglected since they are located out of COI. The peaks of global coherence between precipitation and ENSO are 0.42, 0.35, and 0.44 at 0.5-, 1-, and 2.5-year time scales, respectively (Table 2).

The wavelet coherence between precipitation and PDO (Fig. 7c) shows intermittent significant regions at time scales of 0.5 year (1960, 1962, 1975–1977, 1979, 1985 and 2007) with the in-phase relation occurring over 1975–1977 and of 1-year (1973–1975 and 1990–1994). The 1-year band is found over the period 1973–1975 and 1990–1994 with in-phase correlation. Still there are significant regions at 10- and 16-year time scales, but they are neglected because they are out of COI. The peaks of global coherence between precipitation and PDO are 0.39, and 0.53 at 0.5, and 1-year time scales, respectively (Table 2).

The previous results reveal that the monsoons (ISM, WNPM and EASM) have striking continuous significant regions of wavelet coherence with precipitation at 1-year time scale, and top two global coherence coefficients are 0.97 for ISM and EASM, and 0.96 for WNPM (Fig. 6a–c). Meanwhile the intermittent significant regions at 0.5-, 2.5- and 3.5-year time scales are observed in wavelet coherence between precipitation and monsoons. Thus the monsoons strongly affect precipitation at intra-annual, annual, and inter-annual time scales. The conclusions are consistent with those obtained by Wu and Liu (2005) that monsoon is strongly correlated with precipitation in northern China.

In the climate teleconnections, IOD has intermittent significant regions of wavelet coherence with precipitation at 8-year time scale (Fig. 7a). Simultaneously the intermittent significant regions at 1- and 2- year time scales are observed in wavelet coherence between precipitation and IOD. The global wavelet coherence coefficients at 1-, 2-, and 8-year time scales are 0.44, 0.37, and 0.75 respectively. Thus, IOD impacts the precipitation at annual and inter-annual time scales. The conclusions are consistent with those made by Yang and Guan (2007) that IOD has significant impacts on precipitation in northern China. ENSO has intermittent significant regions in wavelet coherence with precipitation at 0.5-, 1-, and 2.5-year time scales (Fig. 7b). The global wavelet coherence coefficients at 0.5-, 1-, and 2.5-year time scales are 0.42, 0.35, and

0.44, respectively. Therefore, ENSO influences precipitation at intra-annual, annual, and inter-annual time scales. These conclusions are coincident with Li and Zhao's (2000) who investigate the effects of ENSO on the autumn rainfall in northwest China, and their results indicate the presence of obvious inverse correlation between precipitation and ENSO. PDO has intermittent significant regions in wavelet coherence with precipitation at 0.5- and 1-year time scales (Fig. 7c). The global wavelet coherence coefficients at 0.5-, and 1-year time scale are 0.39 and 0.53, respectively. PDO is a multi-decade climate index, however, any significant regions larger than 10 year time scale are not found in wavelet coherence analysis. On the other hand, the global wavelet coherence coefficients at 0.5-, and 1-year time scales are small. So we conclude that the impacts of PDO on precipitation are weak in the NKS Basin.

4.5 Coherence between the spring discharge and climate indices

We calculate the wavelet coherence coefficients and global coherence coefficients between the monthly spring discharge and climate indices. The results are shown in Figs. 8, 9 and 10.

Figure 8a illustrates the wavelet coherence coefficients and the global coherence coefficients between the spring discharge and ISM. From Fig. 8a we can see two groups of significant regions at 0.5-, and 1-year time scales, respectively. The significant regions at 1-year time scale are apparently found in the periods of 1962–1966, 1972–1973, 1976–1978, 1982, 1985–1986, 1995–1996 and 1999–2010. The corresponding peak of global coefficient is 0.62 (Table 3). The significant regions at 0.5-year time scale are observed in the periods of 1963–1964, 1967–1968, 1971–1972, 1976, 1980, 1987, 1989 and 1994 with the in-phase relation occurring over 1987 and 1989. The corresponding local peak of global coefficient is 0.44 (Table 3). So ISM strongly affects the spring discharge at seasonal and annual time scales.

The wavelet coherence coefficients and global coherence coefficients between spring discharge and WNPM are shown in Fig. 8b. There are two groups of significant regions at 1- and 3.5-year time scales, respectively. The significant regions at 1-year time scale are apparently found during 1962–1966, 1972–1973, 1976–1979, 1985–1986, 1995–1997 and 2000–2010. The corresponding peak of global coefficient is 0.63 (Table 3). The in-phase relation at this scale is found over 1985–1986. The significant regions at 3.5-year time scale are observed in the period of 1964–1970. The corresponding local peak of global coefficient is 0.44 (Table 3). So WNPM obviously affects the spring discharge at annual and inter-annual time scales.
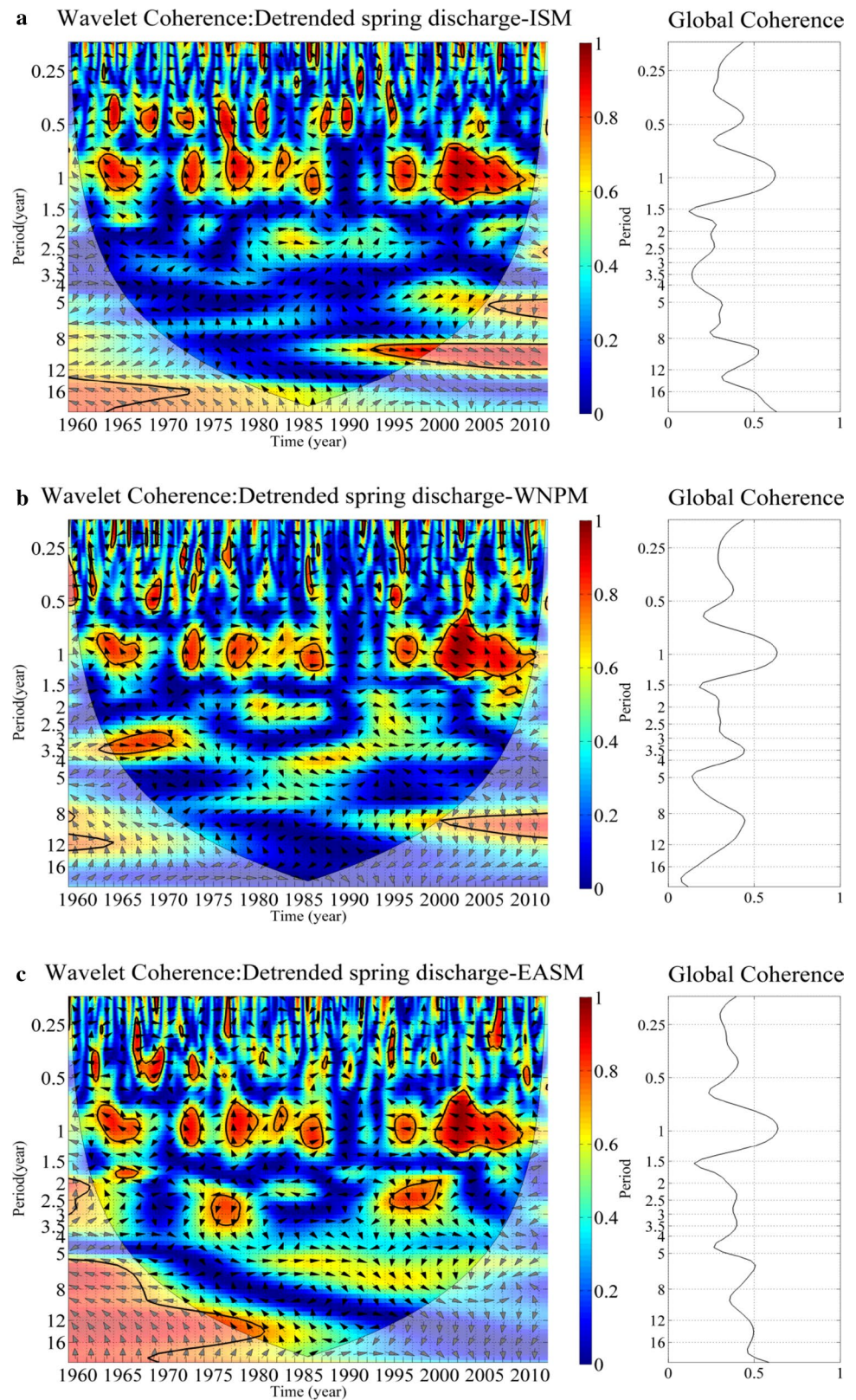
The wavelet coherence between the spring discharge and EASM is shown in Fig. 8c. Three groups of significant regions at 0.5-, 1- and 3.5-year scale bands are observed intermittently. The significant regions at 0.5-year scale band are apparently found in the periods of 1962, 1965–1967, 1972 and 1994. The corresponding peak of global coherence coefficient is 0.41. The significant regions at 1-year scale band are observed in the periods of 1962–1966, 1972–1973, 1976–1979, 1982, 1985–1986, 1995–1996 and 2000–2008 with the corresponding local peak of global coherence coefficient of 0.64. The intermittent significant regions at 3.5-year scale band are observed during the time periods of 1975–1977 and 1995–1999 with the peak of global coherence coefficient of 0.39 (Table 3).

The wavelet coherence coefficients and global coherence coefficients between the spring discharge and IOD in Fig. 9a indicates that spring discharge responses to the variability of IOD at three characteristic scales, 1-year, 3.5–4-year (centering on 4-year) and 5–8-year time scales. The significant region at 1-year time scale is found during 2005–2008. The corresponding peak of global coefficient is 0.29 (Table 3). At 4-year time scale, the significant region is observed during 1995–1996, and the corresponding peak of global coefficient is 0.41 (Table 3). The significant region at 5–8 year time scale is found during 1985–1988. The corresponding peak of global coefficient is 0.48 (Table 3). Thus, IOD influences the spring discharge at annual and inter-annual time scales.

The wavelet coherence coefficients and the global coherence coefficients between the spring discharge and ENSO are shown in Fig. 9b. The significant regions are mainly distributed in the 0.5-year, 1-year and 3.5-year time scales. The significant regions at 0.5-year time scale are found during 1964, 1980–1981 and 1995. The corresponding peak of global coefficient is 0.34 (Table 3). The significant region at 1-year time scale is found during 1978–1980. The corresponding peak of global coefficient is 0.32 (Table 3). The significant region at 3.5-year time scale is found during 1986–1995. The corresponding peak of global coefficient is 0.46 (Table 3). In other words, ENSO impacts the spring discharge on seasonal, annual, and inter-annual time scales.

The wavelet coherence coefficients and global coherence coefficients between spring discharge and the PDO show that the significant regions concentrate on 1-year and 2-year time scales (Fig. 9c). The significant regions at 1-year time scale are found during 1971–1973, 1984–1986, 1995–1997 and 2000–2001. The corresponding peak of global coefficient is 0.40 (Table 3). The significant regions at 2-year fluctuation are mainly found in 1962–1963 and 1992–1994. The corresponding peak of global coefficient is 0.35 (Table 3). PDO as a multi-decade climate index, however, is found to have the significant regions with the

Fig. 8 The wavelet coherence between the detrended spring discharge and the monsoon indices

spring discharge only at 1- and 2-year time scales. These results indicate the impact of PDO on the spring discharge is weak.

Figure 10 illustrates the wavelet coherence between the spring discharge and precipitation. The significant regions are mainly distributed in the 0.5-year, 1-year and 5–8-year

Fig. 9 The wavelet coherence between the detrended spring discharge and the climate indices
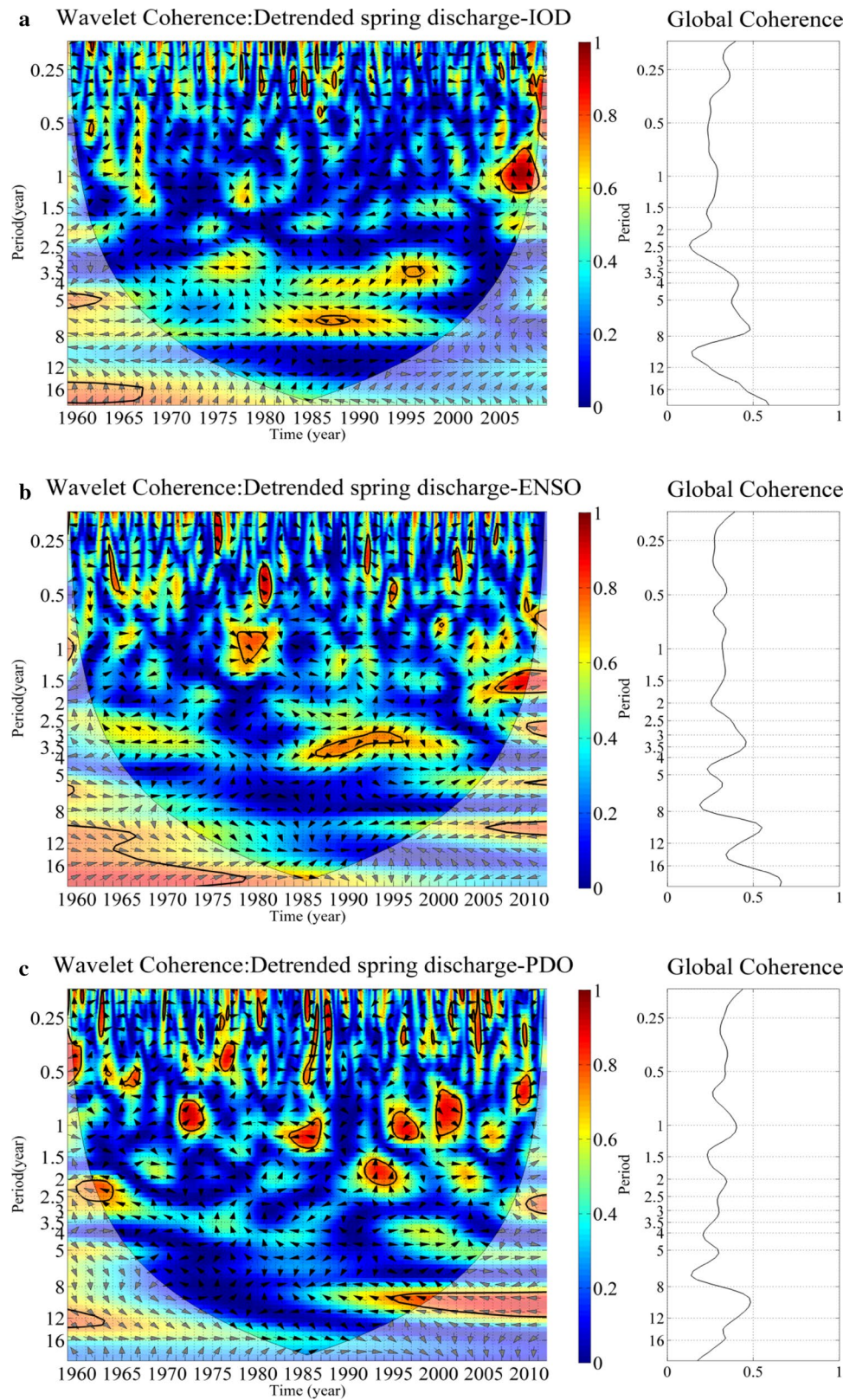
bands (centering on 6.5-year). The significant regions at 0.5-year time scale are found over 1963–1964, 1966–1967, 1971–1972, 1976–1977, 1985–1986, 1995 and 2003–2004.

The in-phase correlation is found in 1985–1986 and the anti-phase correlation is observed in 2003–2004. The corresponding peak of global coefficient is 0.46 (Table 3). The
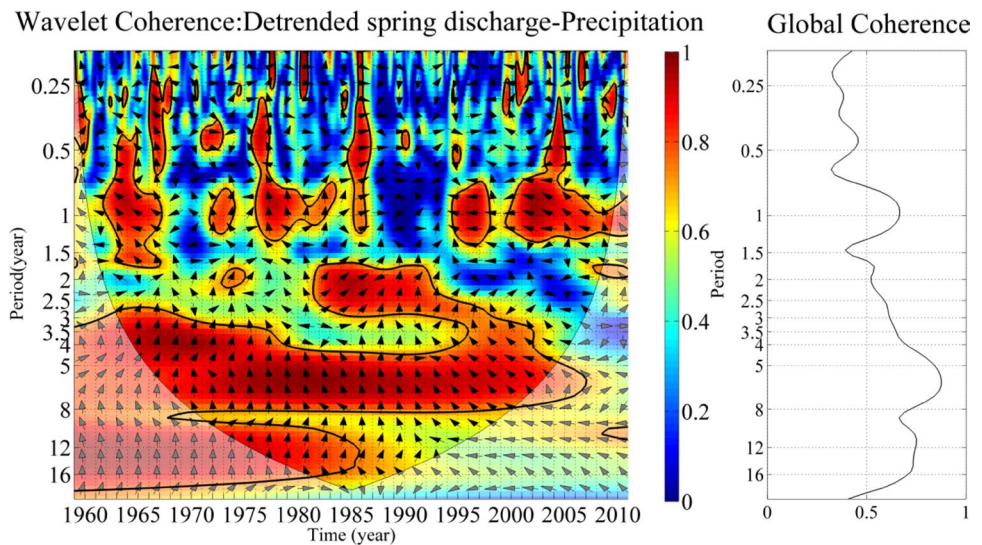
Table 3 Peaks of global coherence coefficients between the detrended spring discharge and climate indices

Time scale of significant region (years)	0.5	1	2	3.5	4	5–8
Monsoon						
ISM	0.44	0.62	–	–	–	–
WNPM	–	0.63	–	0.44	–	–
EASM	0.41	0.64	–	0.39	–	–
Climate teleconnection						
IOD	–	0.29	–	–	0.41	0.48
ENSO	0.34	0.32	–	0.46	–	–
PDO	–	0.40	0.35	–	–	–
Weather						
Precipitation	0.46	0.67	–	–	–	0.88

significant regions at 1-year fluctuation are mainly found during 1962–1966, 1972–1973, 1976–1982, 1985, 1995–1997 and 2000–2009. The corresponding peak of global coefficient is 0.67 (Table 3). The anti-phase relation in the 1-year scale band is found over 1995–1997 and 2000–2002, and the in-phase relation is also found in 1985–1986. The significant regions at 5–8-year time scale are found in the whole period. The corresponding peak of global coefficient is 0.88 (Table 3). Therefore, the spring discharge strongly responds to precipitation at seasonal, annual, and inter-annual time scales.

5 Discussions

The study results indicate that both the monsoons and climate teleconnections affect precipitation in the NKS Basin, and their effects on precipitation vary with time scales. Comparing the wavelet coherence coefficients of precipitation with monsoons to that of precipitation with climate teleconnections, we find that the coefficients of

monsoons are much larger than that of climate teleconnections (Figs. 6, 7; Table 2). The results indicate that the precipitation is more strongly affected by monsoons than by climate teleconnections. In the monsoon indices, ISM, WNPM and EASM impact on precipitation almost at same time scales and in equivalent strength, because coherence coefficients of ISM, WNPM and EASM with precipitation are very close (Fig. 6; Table 2). The monsoons is the dominate factor to precipitation in the NKS Basin.

For the climate teleconnections, the indices influence precipitation in multiple time scales (Fig. 7; Table 2). IOD impacts precipitation at annual and inter-annual time scales. ENSO affects precipitation at multiple time scales, including intra-annual, annual, and inter-annual time scales. The time scales where PDO influences precipitation do not reflect its major fluctuation characteristics (i.e. decadal oscillation). So the effects of PDO on precipitation are weak. The climate teleconnections affect precipitation in the NKS Basin in diversified time scales in relatively weak strength.

In summary, the effects of the monsoons on precipitation are stronger than that of the climate teleconnections. Because precipitation is the main source to recharge groundwater in the NKS Basin, those climate indices which strongly affect precipitation would also be the indices impacting on spring discharge.

The reach of climate effect to spring discharge has to overcome the resistance of heterogeneous aquifers. During the groundwater flow process, the climate signals will be attenuated, delayed, merged, and changed. Thus, the coherence coefficients between the monsoons and spring discharge are much smaller than those between monsoons and precipitation (Figs. 6, 8; Tables 2, 3). The time scales that the monsoons resonate with spring discharge are not the same as those with precipitation (Tables 2, 3). Similarly, the coherence coefficients between teleconnections and spring discharge are much smaller than those between teleconnections and precipitation (Figs. 7, 9; Tables 2, 3). The time scales that teleconnections resonate with spring discharge are not the same as those of the teleconnections resonate with precipitation (Tables 2, 3).

The effects of climate teleconnections on the spring discharge are transmitted and realized by precipitation since precipitation is very closely related to spring discharge (Fig. 10; Table 3). However, the time scales that precipitation resonates to spring discharge are different from those of precipitation to climate indices because of the role of an aquifer in hydrological processes. An aquifer will adjust rhythm or fluctuation of precipitation when the precipitation infiltrates through it, and groundwater is endowed with new periodicity when it discharges to surface as a spring.

6 Conclusions

From the above study results, we conclude that both the monsoons and the climate teleconnections affect precipitation in the NKS Basin. But the time scales of the monsoons resonating with precipitation are concentrated and strong, and those of the climate teleconnections are diversified and relatively weak. So the monsoons are the major factors to precipitation, meanwhile the climate teleconnections also affect precipitation in the NKS Basin.

The effects of the monsoons on the spring discharge are stronger than those of the climate teleconnections. Because the climate signals have to overcome the resistance of heterogeneous aquifers before reaching to the spring, the strong climate signals (e.g. monsoons) have more energy to penetrate through aquifers and act on spring discharge.

Karst aquifers play a vital role in hydrological processes, especially in relations between climate change and groundwater. Climate change impacts precipitation through atmospheric circulation, and precipitation affects groundwater by infiltration and groundwater propagation, and groundwater discharges at the spring. During the processes, the climate signals will be attenuated, delayed, merged, and changed by karst aquifers. Therefore, the fluctuation of the spring discharge is not coincident with that of precipitation in most situations. Only the strong signals can penetrate through aquifers and show their variation characteristics in the spring discharge, but most of the signals will be adjusted by karst aquifers.

Karst aquifers are, in general, highly heterogeneous. Different observation wells may have significantly different groundwater levels in a karst aquifer. It is difficult, and sometimes impossible, to find a "representative" groundwater level as the proxy of a karst aquifer. In another word, the groundwater level measured at a particular location is a "localized" quantity, and does not represent a regional behavior of a karst aquifer. On the other hand, a karst spring is a natural discharge point of an aquifer, and its discharge variation reflects the combined information of permeability and groundwater level change in the aquifer over a regional scale. Thus, spring discharge is a better proxy for groundwater resource variability at a regional scale, and is more closely related to climate variation. In general, the methods developed in this study could be applied to many other karst springsheds in the Northern China. This study makes a solid step towards using meteorological variation to predict groundwater resource variation.

References

Appenzeller C, Stocker TF, Anklin M (1998) North Atlantic oscillation dynamics recorded in Greenland ice cores. Science 282:446–449

Beynen P, Feliciano N, North L, Townsend K (2007) Application of a karst disturbance index in Hillsborough County, Florida. Environ Manag 39(2):261–277

China Preparatory Committee for United Nations Conference on Sustainable Development (2012) The People's Republic of China National Report on sustainable development. People's Publishing House, Beijing

Ford DC, Williams PW (2007) Karst hydrogeology and geomorphology. Wiley, Chichester

Gams I, Nicod J, Julian M, Anthory E, Sauro U (1993) Environmental change and human impacts on the Mediterranean karsts of France, Italy and the Dinaric Region. In: Williams PW (ed) Karst terrians: environmental changes, human impact: catena supplement 25. Catena Verlag, Cremlingen-Destedt, Germany

Gedalof Z, Smith DJ (2001) Interdecadal climate variability and regime-scale shifts in Pacific North America. Geophys Res Lett 28:515–1518

Grinsted A, Moore JC, Jevrejeva S (2004) Application of the cross wavelet transform and wavelet coherence to geophysical time series. Nonlinear Process Geophys 11(5/6):561–566

Guo Q, Wang Y, Ma T, Li L (2005) Variation of karst springs discharge in recent five decades as an indicator of global climate change: a case study at Shanxi, northern China. Sci China D Earth Sci 48(11):2001–2010

Gurdak JJ, Hanson RT, McMahon PB, Bruce BW, McCray JE, Thyne GD, Reedy RC (2007) Limate variability controls on unsaturated water and chemical movement, High Plains Aquifer, USA. Vadose Zone J 6(2):533–547. doi:10.2136/vzj/2006.0087

Han X, Lu R, Li Q (1993) Karst water system: a study on big karst spring in Shanxi. Geological Publishing House, Beijing **(in Chinese)**

Hanson RT, Newhouse MW, Dettinger MD (2004) A methodology to assess relations between climatic variability and variations in hydrologic time series in the southwestern United States. J Hydrol 287(1):252–269

Hartmann A, Goldscheider N, Wagener T, Lange J, Weiler M (2014) Karst water resources in a changing world: review of hydrological modeling approaches. Rev Geophys 52:218–242. doi:10.1002/2013RG000443

Heinz B, Birk S, Liedl R, Geyer T, Straub KL, Andresen J, Bester K, Kappler A (2008) Water quality deterioration at a karst spring (Gallusquelle, Germany) due to combined sewer overflow: evidence of bacterial and micro-pollutant contamination. Environ Geol 57(4):797–801

Holman IP, Rivas-Casado M, Bloomfield JP, Gurdak JJ (2011) Identifying non-stationary groundwater level response to North Atlantic ocean-atmosphere teleconnection patterns using wavelet coherence. Hydrogeol J 19:1269–1278. doi:10.1007/s10040-011-0755-9

Hu C, Hao Y, Yeh T-CJ, Pang B, Wu Z (2008) Simulation of spring flows from a karst aquifer with an artificial neural network. Hydrol Process 22(5):596–604

Intergovernmental Panel on Climate Change (IPCC) (2007) Climate change 2007: synthesis report. IPCC, Geneva, Switzerland

Intergovernmental Panel on Climate Change (IPCC) (2012) Summary for policy makers. In: Field CB et al (eds) Managing the risks of extreme events and disasters to advance climate change adaptation. Cambridge University Press, Cambridge

Jemcov I (2007) Water supply potential and optimal exploitation capacity of karst aquifer systems. Environ Geol 51(5):767–773

Kriechbaumer T, Angus A, Parsons D, Casado MR (2014) An improved wavelet-ARIMA approach for forecasting metal prices. Resour Policy 39:32–41

Kuss AJM, Gurdak JJ (2014) Groundwater level response in U.S. principal aquifers to ENSO, NAO, PDO and AMO. J Hydrol 519:1939–1952

Labat D (2010) Cross wavelet analyses of annual continental freshwater discharge and selected climate indices. J Hydrol 385(1–4):269–278

Leibundgut C (1998) Vulnerability of karst. In: Karsaquiferst Hydrology, vol 247. IAHS Publication, Wallingford, pp 45–60

Li YH, Zhao QY (2000) Effect of ENSO on the autumn rainfall anomaly in northwest China. Clim Environ Res 5(2):205–213 **(in Chinese)**

Liang Y, Han X, Xue F (2008) Water resources conservation for karst spring basin of Sbahxi Provinc. China Water and Power Press, Beijing **(in Chinese)**

Milly PCD, Betancourt J, Falkenmark M, Hirsch RM, Kundzewicz ZW, Lettenmaier DP, Stouffer RJ (2008) Stationarity is dead: whither water management? Science 319(1):573–574

Partal T, Kucuk M (2006) Long-term trend analysis using discrete wavelet components of annual precipitation measurements in Marmara region (Turkey). Phys Chem Earth 32:1189–1200

Perez-Valdivia C, Auchyn D, Vanstone J (2012) Groundwater levels and teleconnection patterns in the Canadian Prairies. Water Resour Res 48:W07516. doi:10.1029/2011WR010930

Sauro U (1993) Human impact on the karst of the Venetian Fore-Alps, Italy. Environ Geol 21(3):115–121

Takio K (2014) Principal component analysis (PCA). In: Katsushi I (ed) Computer vision. Springer, New York, pp 636–639

Taylor R, Scanlon B, Döll P, Rodell M, Beek RV, Wada Y, Longuevergne L, LeBlanc M, Famiglietti J, Edmunds M, Konikow L, Green TR, Chen J, Taniguchi M, Bierkens MFP, MacDonald A, Fan Y, Maxwell RM, Yechieli Y, Gurdak JJ, Allen D, Shamsudduha M, Hiscock K, Yeh PJ-F, Holman I, Treidel H (2013) Groundwater and climate change. Nat Climate Change. doi:10.1038/nclimate1744

Torrence C, Compo GP (1998) A practical guide to wavelet analysis. Bull Am Meteorol Soc 79(1):61–78

Torrence C, Webster PJ (1999) Interdecadal changes in the ENSO-monsoon system. J Clim 12(8):2679–2690

Tremblay L, Larocque M, Anctil F, Rivard C (2011) Teleconnections and interannual variability in Canadian groundwater levels. J Hydrol 410:178–188

Wu C, Liu H (2005) Interdecadal characteristics of the influence of northward shift and intensity of summer monsoon on precipitation over northern China in summer. Plateau Meteorol 24(5):657–665 **(in Chinese)**

Yang X, Guan Z (2007) Role of Indian Ocean Dipole events in the influence of ENSO on the summer rainfall and temperature in China. J Nanjing Inst Meteorol 30(2):170–177 **(in Chinese)**

Yuan C (1982) Calculation of recharge rates of Niangziguan Springs Basin by using Turc equation. Karst and karst groundwater in northern China. Geological Publishing House, Beijing, pp 122–126 **(in Chinese)**